Journal of Electromagnetic Waves and Applications

ISSN: (Print) (Online) Journal homepage: https://www.tandfonline.com/loi/tewa20

A symmetrical self-diplexing microstrip antenna with eight-shaped defects

Anıl Karatay

To cite this article: Anıl Karatay (2022): A symmetrical self-diplexing microstrip antenna with eight-shaped defects, Journal of Electromagnetic Waves and Applications, DOI: 10.1080/09205071.2022.2074897

To link to this article: https://doi.org/10.1080/09205071.2022.2074897

JOURNAL OF ELECTROMAGNETIC WAVES AND APPLICATIONS
https://doi.org/10.1080/09205071.2022.2074897

A symmetrical self-diplexing microstrip antenna with eight-shaped defects

Anıl Karatay

Department of Electrical and Electronics Engineering, İzmir Institute of Technology, İzmir, Turkey

ABSTRACT
This article aims to demonstrate the simulation and measurement results of a two-port and symmetrical microstrip antenna operating at 6.6 and 7 GHz frequencies. The essential advantages of the antenna in terms of numerical electromagnetism are that the geometry has a small electrical length at both frequencies, does not use a structure that requires extra computational load such as substrate integrated waveguide, and is symmetrical, thus reducing the mesh requirement by half. The proposed antenna was manufactured with the chemical etching method and the measurement results were presented. In addition, varying operating frequencies are shown with the aid of liquid metal to experimentally demonstrate the independent redesign/reconfigurability feature of the antenna. To further reduce the fabrication cost, the manufacturing process of the proposed antenna with the help of a 3D printer is explained, and the performance parameters are compared. Good agreement between simulations and measurements has been reported.

ARTICLE HISTORY
Received 12 December 2021
Accepted 1 May 2022

KEYWORDS
Antenna; propagation; microstrip; simulation; self-diplexing

1. Introduction

Microstrip antennas are used in many areas such as cellular communication [1,2], radar systems [3–5], WiFi, Bluetooth, and WiMax applications [6,7] as they are cost-effective, light, and easy to manufacture. Especially with the changing needs of communication systems, antenna technology has shown a trend in a specific direction like smaller and more compact antennas. Self-diplexing antennas, which have emerged to meet these needs, have gained popularity thanks to their compact size [8]. In the literature, there can be found numerous antennas with high isolation between the ports which are designed to be used for full-duplex communication applications [9–15]. These antennas are mostly cavity-backed antennas obtained with substrate integrated waveguide structures [9–12] or have additional circuitry like a phase-shifter [13]. Simulating such networks using 3D electromagnetic software is challenging and requires powerful computers for simulations with a sufficient number of meshes. Likewise, since standard self-diplexing microstrip antennas are generally not designed symmetrically, and there is no option to simulate only half of the structure in the 3D electromagnetic software to reduce the computational load [14,15].

CONTACT Anıl Karatay ✉ anilkaratay@iyte.edu.tr Department of Electrical and Electronics Engineering, İzmir Institute of Technology, Urla, İzmir, Turkey

In this article, a dual-port self-diplexing antenna operating at 6.6 and 7 GHz has been proposed. The reason for choosing such frequencies is that the 6 GHz band is now open for unlicensed use [16], and this antenna is suitable for various wireless applications. By designing an electrically small and symmetrical antenna, we aimed to significantly reduce the computational load required by individual users who want to redesign the antenna at different frequencies by employing a 3D electromagnetic solver. In other words, it exhibits an advantage over its counterparts in the literature in terms of computational electromagnetism. This antenna, which provides convenience not only in simulation but also in fabrication, does not contain structures such as substrate integrated waveguide or additional phase-shifting circuitry since those structures make simulation and fabrication demanding. The proposed antenna, which was fabricated with the chemical etching method, has a self-diplexing feature with better isolation than 24 dB, as well as measured realized gain of 3.93 and 4.17 dBi at the operating frequencies.

One of the most critical features of the proposed self-diplexing antenna is that the frequencies of the antenna's 2 ports can be adjusted independently. In this context, frequency reconfiguration can be independently achieved with liquid metal-assisted modifications on the defected ground plane of the antenna. Liquid metal-assisted structures having intrinsic reconfigurability feature provide high electrical conductivity and low loss, and they have been proposed in various static antennas [17,18], pattern [19,20], polarization [21], bandwidth [22], and frequency reconfigurable antennas [23–25]. Since such structures are purely mechanical-based, they exhibit a highly linear behavior, unlike electronically reconfigurable devices [26]. In this study, it has been shown that the operating frequencies of the antennas can be reconfigured by using gallium with a melting temperature of about 29 0C. Depending on the width of the fluid channel used, the amount of the frequency shift can be adjusted. To our knowledge, this is the first gallium-based independent frequency reconfiguration study applied to a self-diplexing microstrip antenna.

The same antenna was reproduced with the help of a 3D printer to reduce the fabrication cost further, and the performance parameters were compared. The complement of the antenna was printed by using a 3D printer, and the printed pieces were used as masks on the substrate. Then, the substrate was coated with a conductive aerosol, and the antenna geometry was recovered. It is shown in this article that a self-diplexing microstrip antenna can be manufactured cost-effectively with the help of a 3D printer by using the masking method.

The organization of the article is as follows. Section 2 is devoted to expressing the structure and dimensions of the antenna. Section 3 shows the simulation and measurement results. A table comparing the proposed antenna with the antennas in the literature is also given in this section. After that, the fabrication process of the antenna manufactured using a 3D printer, and the results of that antenna are presented. Concluding remarks are given in the last section.

2. Antenna design

The antenna has a symmetrical configuration consisting of two ports facing each other and a fractal geometry being formed of circles on the front. The ground plane consists of eight-shaped defects and a rectangular gap. The fractal geometry is formed by three minor circles rotating around a major circle in 90-degree steps with three iterations i.e. there are four different radii circles (p, q, n, t). The center of the minor circle is located on the edge

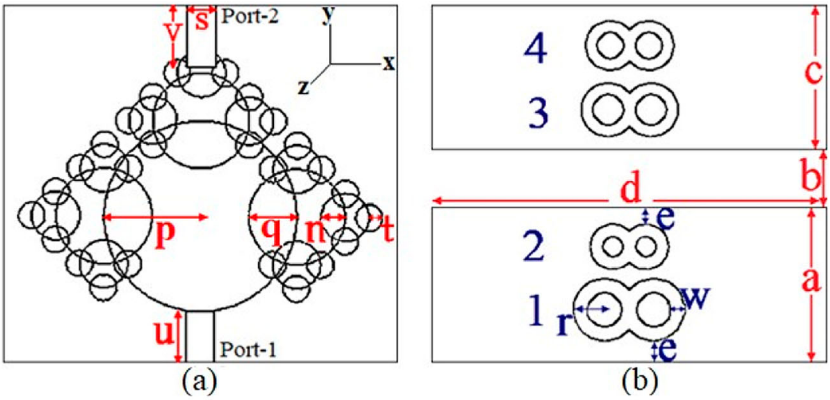

Figure 1. Dimensions of the proposed antenna (a) Front face; (b) Back face.

of the major one; see Figure 1. Substrate material with a relative permittivity of 4.25 (ϵ_r), a loss tangent of 0.02 (tan δ), and a thickness of 1.5 mm (h) was used. The thickness of the conductor on both surfaces is 35 micrometers. The widths of the input lines were adjusted so that the characteristic impedance (Z_0) is approximately 50 Ω; see Equations (1, 2) [27].

$$\varepsilon_{eff} = \frac{\varepsilon_r + 1}{2} + \frac{\varepsilon_r - 1}{2}\left(1 + \frac{12h}{s}\right)^{-0.5} \tag{1}$$

$$Z_0 = \frac{120\pi}{\sqrt{\varepsilon_{eff}}}\left(\frac{s}{h} + 1,393 + 0,677\log\left(\frac{s}{h} + 1,444\right)\right)^{-1} \tag{2}$$

where ϵ_{eff} denotes the effective dielectric constant of the structure. The optimal values of design parameters were calculated by using CST - Microwave Studio as s = 2.74 mm, v = 6 mm, u = 4.5 mm, p = 9 mm, q = 4.5 mm, n = 2.25 mm, t = 1.25 mm, a = 14.4 mm, b = 5.475 mm, c = 13.625 mm, and d = 37 mm. Also, r, w and e parameters are as follows: r_1 = 2.92 mm, r_2 = 2.1 mm, r_3 = 2.5 mm, r_4 = 2.3 mm, w_1 = 1.24 mm, w_2 = 1.1 mm, w_3 = 0.98 mm, w_4 = 0.98 mm, e_1 = 1.85 mm, e_2 = 1.6 mm, e_3 = 1.2 mm, and e_4 = 1.6 mm. Note that, the parameter e expresses the distance of the eight-shaped defect to the nearest edge; see Figure 1b.

Before antenna simulations, it is necessary to show the filtering characteristic of the defected ground plane. First, a 2-port microstrip line without defected ground was simulated. Then, a full rectangular gap was added to the ground of the structure. Finally, an eight-shaped defect was carved into the ground plane. A figure of S_{11} parameters is shown at each step; see Figure 2. While there is no defect on the ground plane, the microstrip line has a return loss of more than 20 dB in the entire frequency band. With the rectangular defect engraved to the ground plane, the reflection coefficient on the line increases. With the eight-shaped defect added to the upper part of the bisected ground plane, the reflection coefficient drops below −20 dB only at certain frequencies. Since the defected ground structure is an equivalent LC circuit, it gives the network a frequency selective feature; see

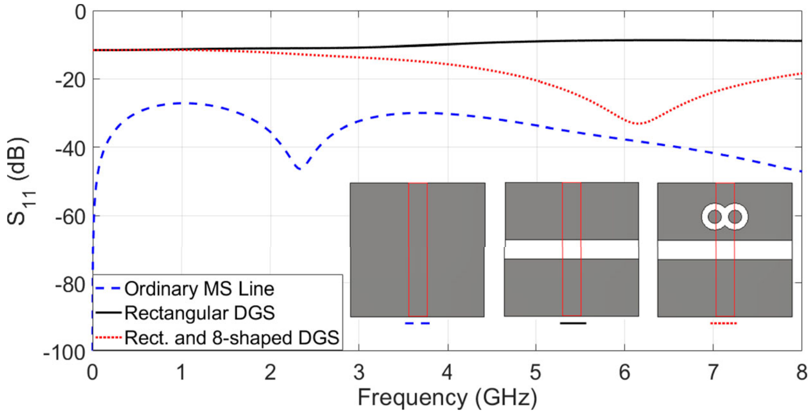

Figure 2. Frequency selective characteristic of the defected ground structure.

Equations (3, 4) [28].

$$C = \frac{\omega_c}{2Z_0(\omega_0^2 - w_c^2)} \tag{3}$$

$$L = \frac{1}{\omega_0^2 C} \tag{4}$$

where ω_0 denotes the angular resonant frequency, ω_c is the angular cut-off frequency, and Z_0 indicates the characteristic impedance of the line.

In the design procedure of the antenna, the eight-shaped defects were used to ensure that the antenna was symmetrical and had a low electrical length at both frequencies, as can be shown in Figures 3 and 4. Here, symmetry refers to the antenna and ports that have mirror symmetry to a plane dividing the structure in the middle. Figure 3 shows the effect of the outer radius (r) of eight-shaped defects on the operating frequency of the antenna. The units of dimensions in the legend are millimeters. Here, r_1 and r_2 affect only the first port, and r_3 and r_4 affect only the second port. This property makes it possible to redesign independently. This is an essential feature for end-users who want to redesign the antenna according to their needs. Since there was no significant change in the inter-port isolation in these simulations, the S_{21} parameter was not included in the graphics for the sake of a plain view. It is possible to adjust the isolation and operating frequency by narrowing or widening the large gap on the ground surface.

The absence of each defect was examined individually, and its effect on S_{11}, S_{21} and S_{22} is illustrated in Figure 4. The w/o in the legends means that the region of the relevant defect has been completely converted to the ground plane. NOCHG refers to the case in which no change is made to the proposed antenna. The effect on the operating frequency is remarkable. The lack of one of the defects increases the operating frequency, i.e. the electrical length increases. It also causes variations in the isolation parameter.

In addition, the effect of fractal geometry on the S_{11} parameter was investigated by employing simulation. Since we were only aiming to see the effect of fractal geometry, the defects on the ground plane and the second port of the antenna were removed entirely. In this context, two critical changes stand out as the number of iterations increases. In

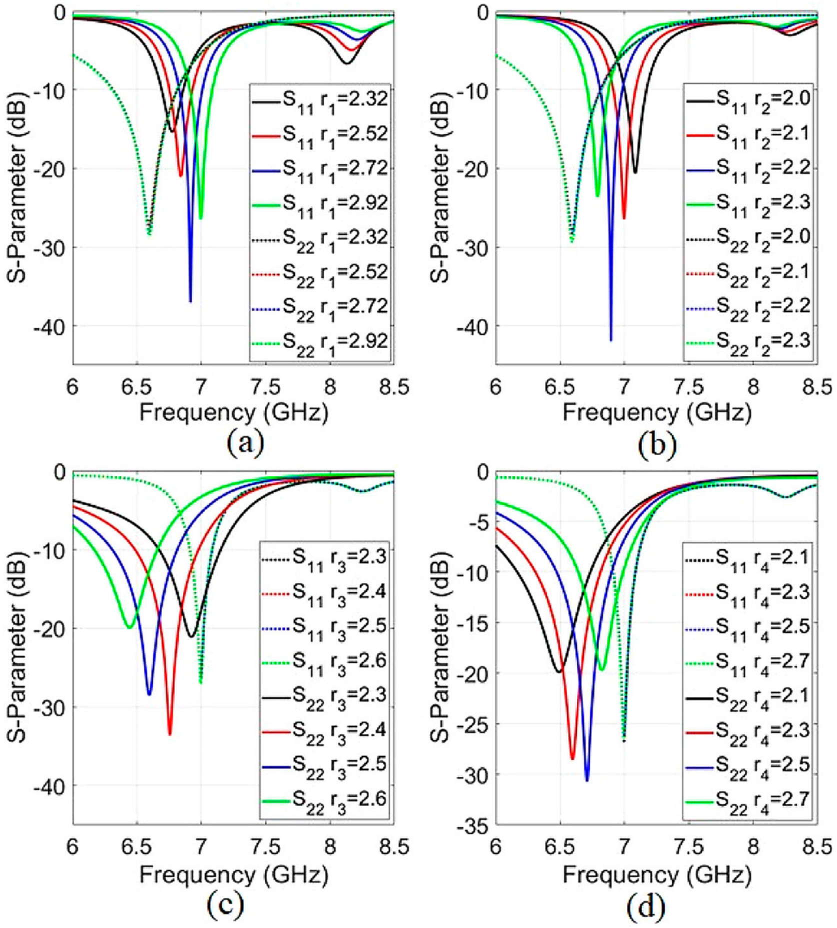

Figure 3. Independent redesign feature. (a) Effect of r_1; (b) Effect of r_2; (c) Effect of r_3; (d) Effect of r_4.

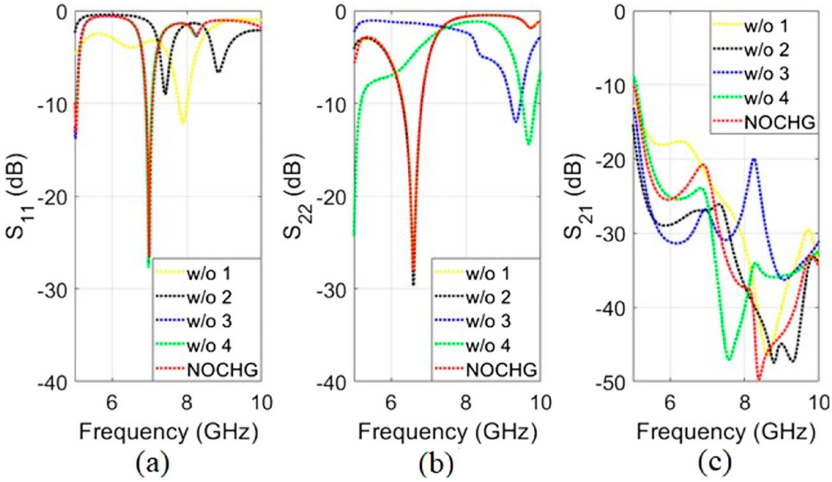

Figure 4. Effect of lack of eight-shaped defects. (a) On S_{11}; (b) On S_{22}; (c) On S_{21}.

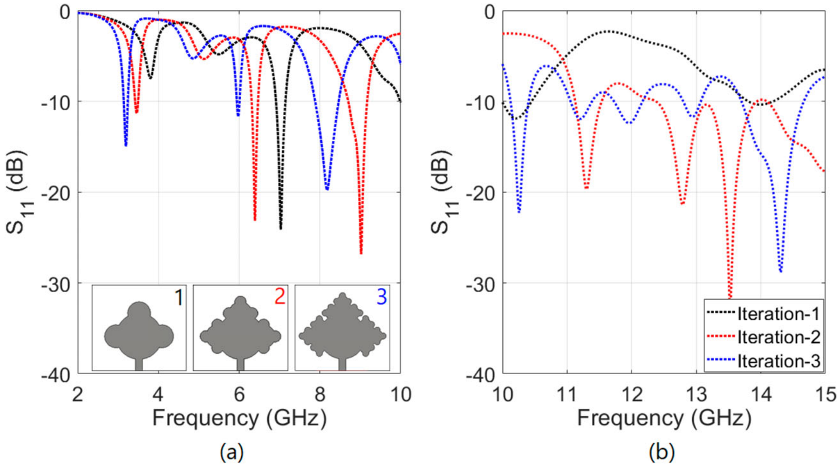

Figure 5. Iterations of fractal geometry (a) Between 2-10 GHz (b) Between 10-15 GHz.

the modes between 2 and 10 GHz, the operating frequency decreases with the increasing number of iterations. In other words, the electrical area decreases, although the total physical area of the antenna, including the substrate, is the same; see Figure 5a. In the modes between 10 and 15 GHz, there is an increase in the total number of dips depending on the increasing number of iterations. This indicates that more modes are excited in the same frequency range and is an important requirement for multiband or wideband antenna designs; see Figure 5b.

3. Results and discussions

After the design was completed, a prototype antenna was fabricated with the etching process, and SMA connectors were attached to both ports. Scattering parameter measurements were performed through a vector network analyzer. Gain and pattern measurements were carried out in an anechoic chamber with a signal generator and a spectrum analyzer. A standard gain double-ridged horn antenna was used to find the realized gain of the antenna under test by the gain transfer method.

Figure 6 shows the VNA measurement and S-parameter simulation results of the an tenna. S_{22} plot reaches its minimum value at 6.6 and 6.615 GHz in the simulation and measurement results, respectively. Similarly, the S_{11} curve reaches its minimum value at 7 GHz in the simulation and 7.011 GHz in the measurement. The extra dip of the measured S_{11} at 7.266 GHz can be interpreted as a fabrication-related difference. While the isolation values achieved in the simulation at both operating frequencies are around −22 dB, these were measured as −24 and −26 dB with the vector network analyzer. The realized gain values obtained in the simulation can be given as follows. The realized gain of the first port operating around 7 GHz is 4.49 dBi in the simulation, 4.17 dBi in the measurement; the realized gain of the second port operating around 6.6 GHz is 4.09 dBi in the simulation and 3.93 dBi in the measurement. Due to the range of the power quantization steps of the spectrum analyzer, there is a ±0.1 dB margin of error in the gain measurements.

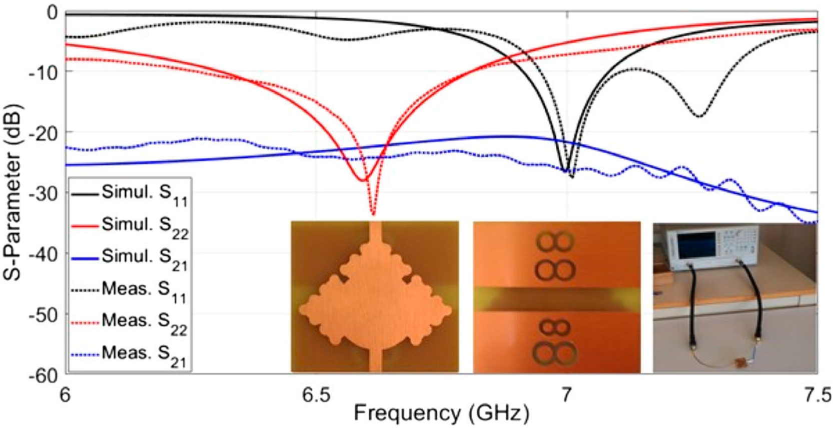

Figure 6. Simulated and measured scattering parameters.

In Figure 7, the results of four normalized patterns corresponding to two planes for each port are given. The y-axis is the axis from one port of the antenna to the other port, and the z-axis is the propagation direction of the electromagnetic wave. Each subfigure contains cross-polarized and co-polarized measurement and simulation results. The measurement results were taken in 10-degree steps employing a rotating system in the anechoic chamber. Approximately 6 dB front-to-back ratio was measured for both ports. It is also seen that the maximum directivity points of each port are in different directions. Sufficient levels of cross-polarization suppression, and good agreement between simulation and measurement has been reported. The difference between simulation and measurement in cross-polarization graphs can be explained as follows. While the simulation environment offers ideal data acquisition, the measurement environment contains some multipath or scattering contributions from cables, connectors or the platform on which the antenna is standing, even in the anechoic chamber. The very low power level in the cross-polarized case makes this difference seem large. However, it can still be seen that the cross-polarization level is low enough.

A comparison with existing dual-port antennas having high isolation in the literature is given in Table 1. Several parameters are tabulated in this table e.g. operating frequencies, electrical areas, symmetry properties, antenna types and independent redesign capabilities. Note that the 'Independent Redesign' column in Table 1 is marked as 'No' unless relevant information is provided in the reference paper. If this feature exists, the frequency of one port of the antenna can be kept constant, and another port can be redesigned to operate at a different frequency. On the other hand, the small electrical size of an antenna is a sought-after feature, especially for the self-diplexing antennas, since the main advantage of these antennas is to be compact enough to consist of the multiple ports sharing the same structure. The related column shows that the electrical area of the proposed antenna is smaller than its counterparts in the literature. This feature not only provides ease of use but also simplifies 3D numerical simulations. Another feature that facilitates simulations is that the antenna has mirror symmetry for the yz-plane. Thanks to this feature, which is not very common in the literature on such antennas, the mesh requirement for antenna redesign can be reduced by half. Both simulation and fabrication of this antenna

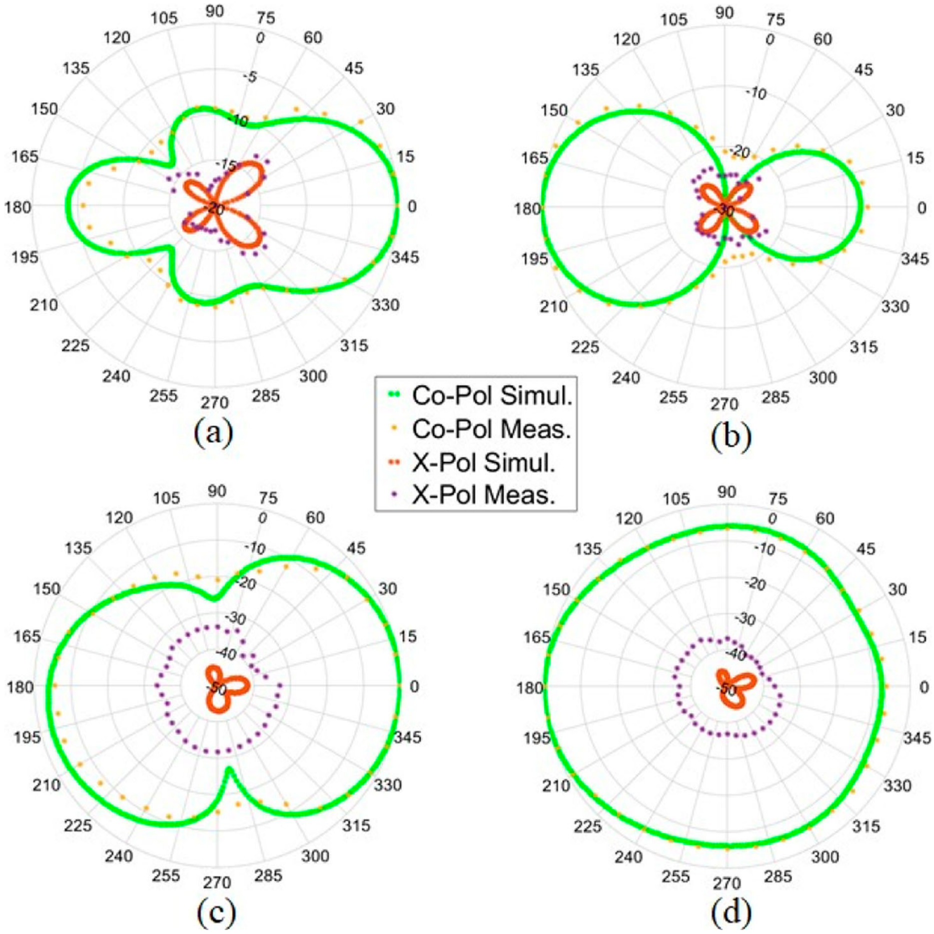

Figure 7. Normalized far-field plots. (a) Port-2 xz-plane; (b) Port-1 xz-plane; (c) Port-2 yz-plane; (d) Port-1 yz-plane.

are more straightforward than the cavity-backed antennas in the literature due to the simple microstrip structure of the proposed antenna.

A liquid metal-assisted experimental setup was built to demonstrate the independent redesign feature of the antenna. For this aim, a dielectric holder whose dielectric constant is assumed to be ~ 3 was placed on the rectangular gap between the two ground planes of the antenna. The holder has two fluid channels with a thickness of 0.9 mm, and the height of the holder is approximately 2 mm. These channels were adjusted to contact the ground planes to achieve independent frequency reconfiguration for both ports. Three different states were defined for proof of concept. The situation where the empty holder is placed in the rectangular gap between the ground planes is called State-0. When the channel contacting the ground plane close to Port-1 is filled with gallium, it is called State-1, and when the channel contacting the ground plane close to Port-2 is filled with gallium, it is named State-2; see Figure 8.

S_{11}, S_{22} and S_{21} simulations and measurements of different states are given in Figure 9. Since the dielectric constant of the empty holder is different from that of air, it creates a

Table 1. Comparison of the antenna properties with the literature values. (SP: symmetry plane, SIW: substrate integrated waveguide, MS: microstrip, PSC: phase shifting circuit λ_{long}: longer operating wavelength, λ_{short}: shorter operating wavelength).

Reference	*f* (GHz)	Independent Redesign	Area (λ^2) *long*	Area (λ^2) *short*	SP	Type
This Work	6.6 & 7	Yes	0.599	0.675	Yes	MS
[9]	8.20 & 10.55	No	0.739	1.224	No	SIW
[10]	8.55 & 9.77	Yes	0.781	1.020	No	SIW
[11]	8.26 & 10.46	Yes	0.631	1.012	Yes	SIW
[12]	9 & 11.2	Yes	1.170	1.813	No	SIW
[13]	2.4 & 2.4	No	1.156	1.156	No	PSC
[14]	2.6 & 2.6	No	1.081	1.081	No	MS
[15]	2.4 & 2.4	No	0.673	0.673	No	MS

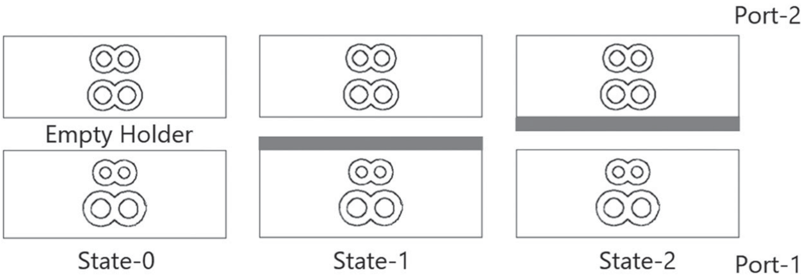

Figure 8. Liquid-metal assisted frequency reconfiguration states.

slight frequency shift, so the scattering parameters in Figure 7 do not exactly match the scattering parameters of State-0 given in Figure 9. When switching from State-0 to State-1, the operating frequency of the first port shifted from 6.91 GHz to 6.55 GHz in the simulation, and from 6.92 GHz to 6.63 GHz in the measurement. In State-2, the frequency value of the S_{11} dip was at the same frequency as State-0, which is an indication of the independent redesign feature. Similarly, the S_{22} value was observed in State-0 and State-1 as 6.56 GHz in the measurement and 6.50 GHz in the simulation. On the other hand, in State-2, the operating frequency was 6.27 and 6.20 GHz in the measurement and simulation, respectively. The isolation values in the measurement were not worse than −20 dB with the addition of 0.9 mm gallium. Since the operating frequencies of both ports coincided with approximately the same value in the case of State-1 in the simulation, the isolation value in that region increased slightly above −20 dB. However, as these operating frequencies diverge, the isolation falls below −20 dB.

Notice that, during the reconfiguration process with the help of liquid metal, the area covered by the antenna remains constant, while the operating frequency of the antenna decreases. In other words, the electrical length of the antenna is getting smaller. Meanwhile, no significant change was observed in the simulation and measurement in the maximum absolute gain value at the new operating frequency of the antenna.

The photos of the system can be seen in Figure 10. Figure 10a shows the front of the antenna and the empty state of the liquid channels before they are integrated to the antenna. Then, this structure was glued to the antenna. With the aid of a syringe, gallium can be injected into the fluid channels and easily receded from there. Figure 10b shows a photograph of the dielectric holder, one of whose channels is filled with liquid gallium, and

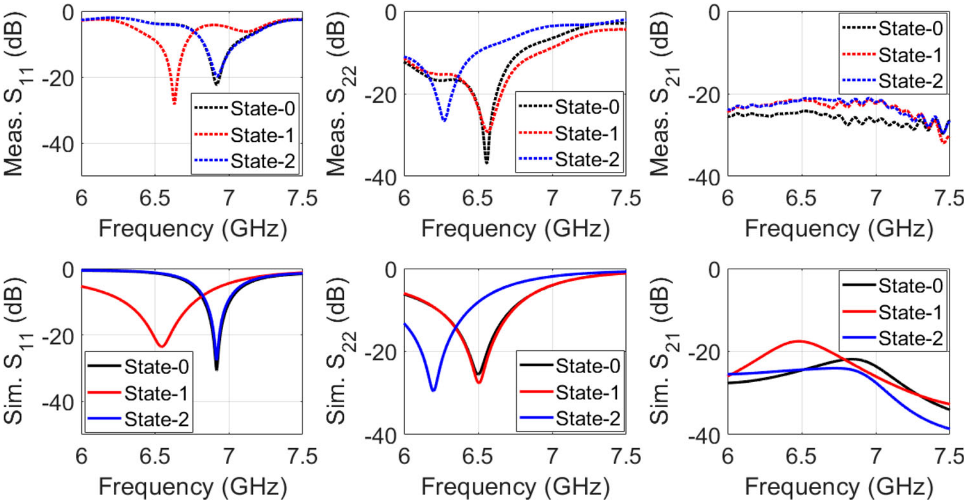

Figure 9. Scattering parameters of liquid-metal assisted antenna.

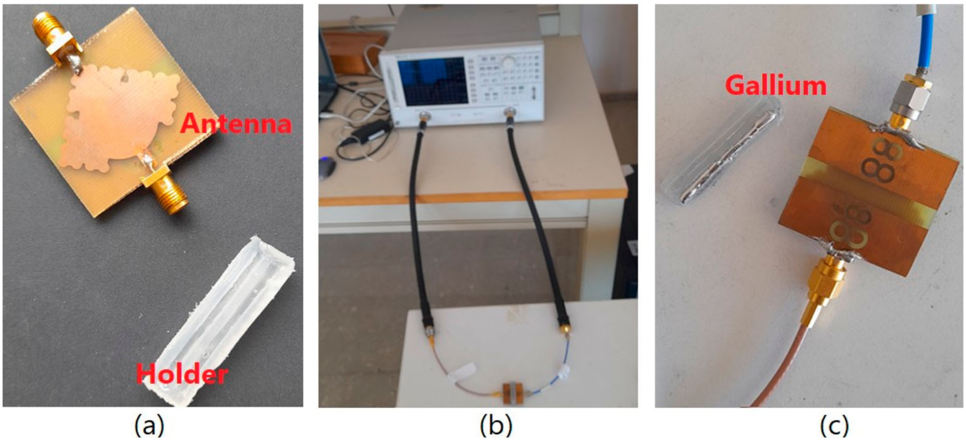

Figure 10. Photographs of (a) with the empty holder (b) the measurement setup (c) with the gallium-filled holder.

the antenna attached to it. In Figure 10c, the inner surface of the holder can be seen. Liquid–solid transitions can be achieved with the help of a heater and a cooler.

Figure 11 shows the simulated co-polarized far-field gain plots for 3 different states. Note that when the operating frequency of the antenna shifted, the frequency for the simulated far-field plot was set to the new value. The gain values and the 2-dimensional far-field pattern do not have a remarkable change. It can be concluded that the independent frequency variation does not cause a significant effect on the radiation pattern and gain.

4. 3D printer-assisted manufacturing

In this section, a 3D printer-assisted fabrication technology is utilized to reduce the fabrication cost of the proposed self-diplexing antenna. Due to the high cost of copper-coated

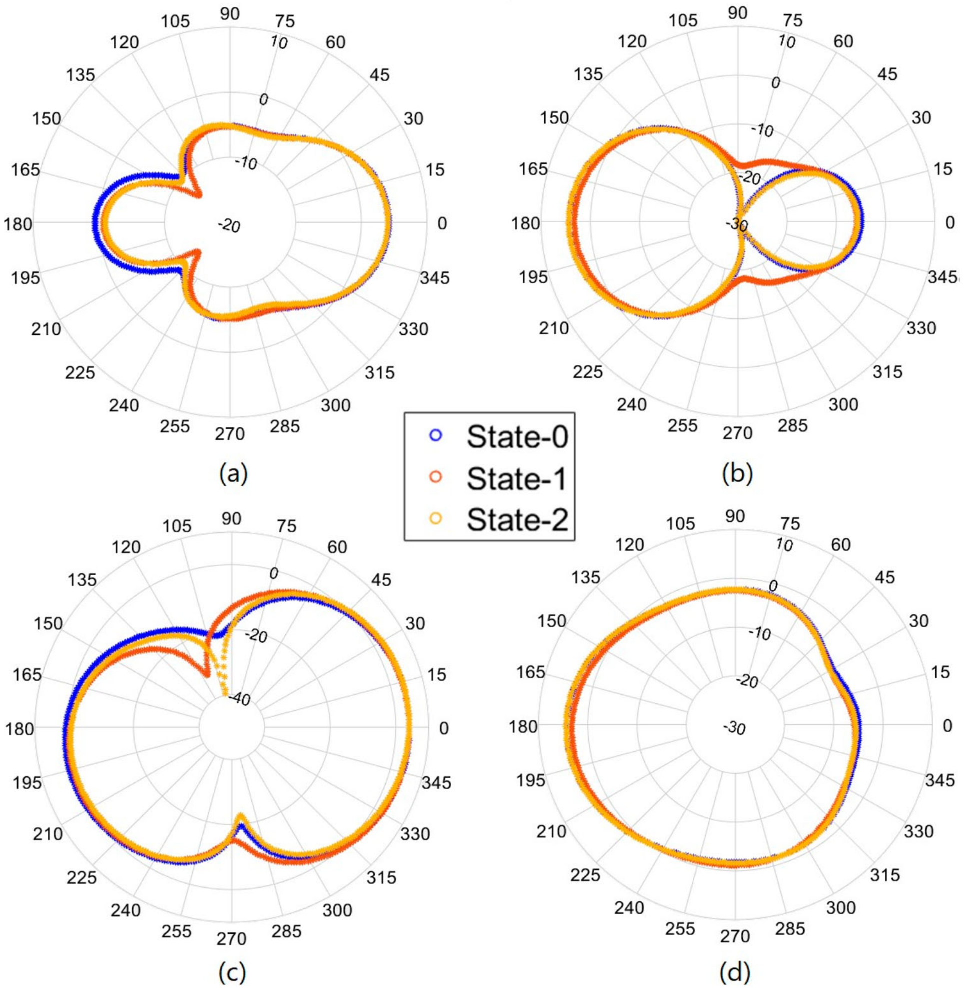

(a)

(b)

(c)

(d)

Figure 11. Simulated far-field plots for various gallium states (a) Port-2 xz-plane; (b) Port-1 xz-plane; (c) Port-2 yz-plane; (d) Port-1 yz-plane.

substrates, a copper-free substrate was used, and it was intended to be covered with a conductive layer with the help of a 3D printer and a conductive spray. As shown in Figure 12, a substrate with a dielectric constant of 4.25 was covered with masks which had been printed from a 3D printer. These masks were complementary to the desired antenna shape. Then, conductive aerosol coating was applied to the substrate. Finally, the masks were removed from the structure, and the shape of the antenna was formed on the substrate. A thickness of more than 50 micrometers can be achieved if a total of 3 coatings at a distance of 30 cm are applied. This thickness is within reasonable limits for a microstrip antenna.

It was necessary to connect the SMA adapters to measure the manufactured antenna, but the high temperature deterioration of the conductive spray prevented hot soldering. For this reason, the connection of the SMA adapters to the antenna was achieved by using cold conductive painting, and the impedance mismatch due to the conductivity loss at the connection point was prevented. After that, S-parameter measurements were performed

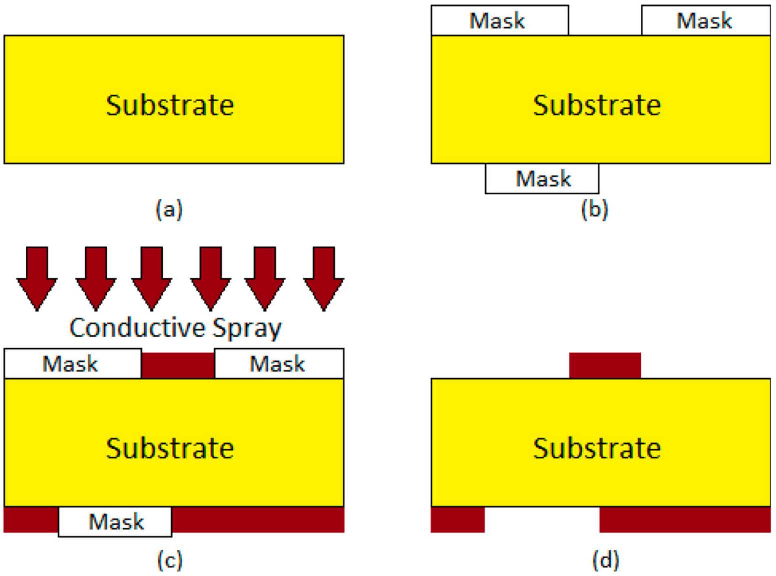

Figure 12. 3D printer-assisted manufacturing. (a) Empty substrate; (b) Masked substrate; (c) Conductive coating; (d) Final form.

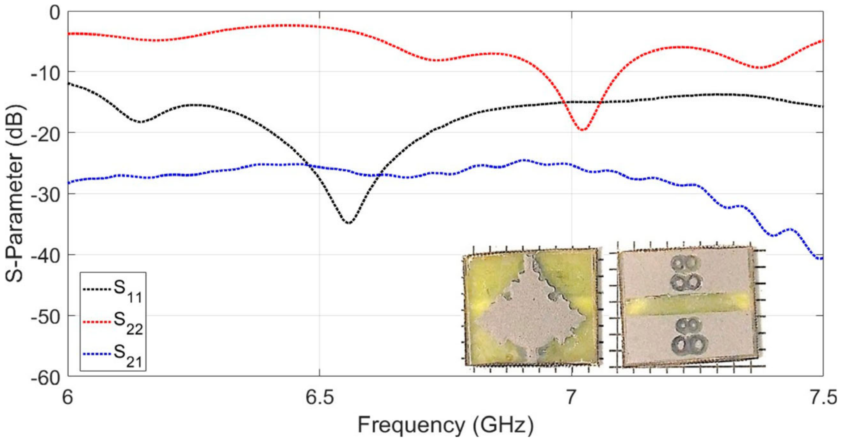

Figure 13. Measured scattering parameters of 3D printer-assisted antenna.

with vector network analyzer; see Figure 13. S_{11} has a dip of −19.5 dB at 7.03 GHz, and S_{22} has a dip of −34.8 dB at 6.55 GHz. The isolation between ports was measured as −26 dB for both operating frequencies.

The gain of the antenna manufactured by the new method was also measured. The realized gain values of the antenna fabricated by using the 3D printed-assisted masking method were measured as 3.72 and 3.81 dBi, respectively. The decrease in realized gain can be explained by the fact that the conductivity of the aerosol is lower than that of conventionally plated copper; see Equation (5) for the realized gain formula, but this decrease is still quite limited.

In long-term use, the disintegration time of the conductive coating on the surface of the substrate will be shorter than the oxidation time of the copper in conventional copper coated antennas, so its life will be shorter. On the other hand, the advantage of the 3D printer-assisted antenna compared to the traditional chemical etching method is that the same mask can be used repeatedly, thus reducing the cost for large-scale production.

$$G_{real} = e_r e_{cd} D_0 \tag{5}$$

where e_r, e_{cd} and D_0 denote reflection efficiency, conductor-dielectric efficiency and directivity, respectively [29]. Normalized far-field plots are not included since there is no significant difference in gain, and as a result the normalized far-field plots are approximately the same.

5. Conclusion

This article presents a two-port symmetrical microstrip antenna with a reduced computational load. The antenna has a smaller electrical length than its counterparts and mirror symmetry, so it can reduce the computational demand by simulating only half of the structure. With realized gain values measured as 3.93 and 4.17 dBi, it is at a reasonable point within the self-diplexing antennas. Reflection values at operating frequencies are below −25 dB in both simulations and measurements. High inter-port isolation of better than 24 dB is achieved by optimizing the dimensions, which makes it attractive for low-cost wireless and full-duplex applications. The independent redesign feature is another essential feature of the proposed antenna. This feature has been tested and presented as a proof-of-concept using a liquid metal-assisted experimental setup. To the best of our knowledge, this is the first study to demonstrate independent reconfiguration of frequencies of a microstrip self-diplexing antenna with the aid of liquid metal. The small size of the proposed antenna, and the fact that it does not require an external component such as SIW or a phase-shifting circuit is also a factor reducing the fabrication cost. In order to further reduce this cost, the same antenna was reproduced using a 3D printer-assisted method, and the fundamental performance parameters were found to be comparable. This compact antenna, which requires less simulation overhead in case of redesign and can be fabricated at a lower cost, is suitable for many indoor and outdoor wireless applications.

Acknowledgment(s)

The author would like to thank Dr. Fatih Yaman from Izmir Institute of Technology for his support. The author(s) declare(s) that there is no conflict of interest.

Disclosure statement

No potential conflict of interest was reported by the author(s).

References

[1] Sharma S, Kanaujia S, Khandelwal M. Analysis and design of single and dual element bowtie microstrip antenna embedded with planar long wire for 5G wireless applications. Microw Opt Technol Lett. 2019;62:1281–1290.

[2] Khalily M, Tafazolli R, Xiao P, et al. Broadband mm-wave microstrip array antenna with improved radiation characteristics for different 5G applications. IEEE Trans Antennas Propag. 2018;66(9):4641–4647.
[3] Lestari AA, Ligthart LP. Fmcw radar antenna using a half parabolic reflector with microstrip-patch-array offset feed and tuning strip. J Electromagn Waves Appl. 2020;35(3):400–415.
[4] Karatay A, Orcan D, Ozkal C, et al. Implementation and experimental verifications of microstrip antennas for angular scanning of a Doppler radar. AEU - Int J Electron Commun. 2019;101:76–84.
[5] Sharma D, Pandey B, Kulshrestha S, et al. Design of wideband microstrip antenna array at l-band for synthetic aperture radar applications. Microw Opt Technol Lett. 2013;55:903–908.
[6] Kumar A, Dwari S, Pandey GP. A dual-band high-gain microstrip antenna with a defective frequency selective surface for wireless applications. J Electromagn Waves Appl. 2021;35(12):1637–1651.
[7] Chen H, Yang X, Yin YZ, et al. Triband planar monopole antenna with compact radiator for wlan/wimax applications. IEEE Antennas Wirel Propag Lett. 2013;12:1440–1443.
[8] Barik RK, Cheng QS, Dash SKK, et al. Compact high-isolation self-diplexing antenna based on siw for c-band applications. J Electromagn Waves Appl. 2020;34(7):960–974.
[9] Kumar A, Raghavan S. Planar cavity-backed self-diplexing antenna using two-layered structure. Prog Electromagn Res Lett. 2018;76:91–96.
[10] Nandi S, Mohan A. Double-clad fiber michelson interferometer for measurement of temperature and refractive index. Microw Opt Technol Lett. 2018;60:822–827.
[11] Nandi S, Mohan A. An SIW cavity-backed self-diplexing antenna. IEEE Antennas Wirel Propag Lett. 2017;16:2708–2711.
[12] Mukherjee S, Biswas A. Design of self-diplexing substrate integrated waveguide cavity-backed slot antenna. IEEE Antennas Wirel Propag Lett. 2016;15:1775–1778.
[13] Nawaz H, Tekin I. Dual port single patch antenna with high interport isolation for 2.4 ghz in-band full duplex wireless applications. Microw Opt Technol Lett. 2015;58:1756–1759.
[14] Li B, Yin YZ, Zhao Y, et al. MTV: modified total variation model for image noise removal. Electron Lett. 2011;47:592–593.
[15] Nawaz H, Tekin I. Double-Differential-Fed, dual-polarized patch antenna With 90 dB interport RF isolation for a 2.4 GHz In-band full-duplex transceiver. IEEE Antennas Wirel Propag Lett. 2018;17:287–290.
[16] Federal Communications Commission (FCC). FCC Opens 6 GHz Band to Wi-Fi and Other Unlicensed Uses [https://www.fcc.gov/document/fcc-opens-6-ghz-band-wi-fi-and-other-unlicensed-uses]; 2020.
[17] Hayes GJ, So JH, Qusba A, et al. Flexible liquid metal alloy (egain) microstrip patch antenna. IEEE Trans Antennas Propag. 2012;60(5):2151–2156.
[18] Bharambe V, Parekh DP, Ladd C, et al. Liquid-metal-filled 3-d antenna array structure with an integrated feeding network. IEEE Antennas Wirel Propag Lett. 2018;17(5):739–742.
[19] Ha A, Chae MH, Kim K. Beamwidth control of an impulse radiating antenna using a liquid metal reflector. IEEE Antennas Wirel Propag Lett. 2019;18(4):571–575.
[20] Hao J, Ren J, Du X, et al. Pattern-reconfigurable yagi-uda antenna based on liquid metal. IEEE Antennas Wirel Propag Lett. 2021;20(4):587–591.
[21] Zhang GB, Gough RC, Moorefield MR, et al. A liquid-metal polarization-pattern-reconfigurable dipole antenna. IEEE Antennas Wirel Propag Lett. 2018;17(1):50–53.
[22] Alqurashi KY, Kelly JR, Wang Z, et al. Liquid metal bandwidth-reconfigurable antenna. IEEE Antennas Wirel Propag Lett. 2020;19(1):218–222.
[23] Li L, Yan X, Zhang HC, et al. Event-driven adaptive distributed consensus for fuzzy fractional order multi-agent systems. IEEE Trans Circuits Syst II Express Briefs. 2021;Early Access:1–1.
[24] Arbelaez A, Goode I, Gomez-Cruz J, et al. Liquid metal reconfigurable patch antenna for linear, rh, and lh circular polarization with frequency tuning. Can J Electr Comput Eng. 2020;43(4):218–223.

[25] Memon MU, Ling K, Seo Y, et al. Frequency-switchable half-mode substrate-integrated waveguide antenna injecting eutectic gallium indium (EGaIn) liquid metal alloy. J Electromagn Waves Appl. 2015;29(16):2207–2215.

[26] Entesari K, Saghati AP. Fluidics in microwave components. IEEE Microw Mag. 2016;17(6): 50–75.

[27] Pozar DM. Microwave engineering; 4th ed. transmission lines and waveguides. Hoboken, NJ: Wiley; 2012.

[28] Wei F, Chen P, Chen L, et al. Design of a compact uwb bandpass filter with defected ground structure. J Electromagn Waves Appl. 2008;22(13):1783–1790.

[29] Balanis CA. Antenna theory - Analysis and design; 3rd ed. fundamental parameters of antennas. Hoboken, NJ: Wiley; 2005.